Granular Matter (2024) 26:28
https://doi.org/10.1007/s10035-024-01395-6

ORIGINAL REPORT

# Contact rheological DEM model for visco-elastic powders during laser sintering

J. E. Alvarez[1] · A. H. Nijkamp[1] · H. Cheng[1,2] · S. Luding[1] · T. Weinhart[1]

Received: 25 September 2023 / Accepted: 3 January 2024


**Abstract**
Laser sintering is a widely used process for producing complex shapes from particulate materials. However, understanding the complex interaction between the laser and particles is a challenge. This investigation provides new insights into the sintering process by simulating the laser source and the neck growth of particle pairs. First, a multi-physics discrete element method (DEM) framework is developed to incorporate temperature-dependent contact rheological and thermal properties, incorporating heat transfer and neck formation between the particles. Next, energy transport by ray tracing is added to allow for computing the amount of laser energy absorbed during sintering. The DEM model is calibrated and validated using experimental data on neck growth and temperature evolution of particle pairs made of polystyrene and Polyamide 12. The findings show that the proposed DEM model is capable of accurately simulate the neck growth during the laser sintering paving the way for better controlling and optimizing the process.

**Keywords** Discrete element method · Laser beam absorption · Neck growth · Sintering · Polymers

## 1 Introduction

Laser sintering (LS) is an additive manufacturing technique that offers cost-efficient production of complex geometries and a variety of material options, including metals, ceramics, and polymers. The use of LS for polymer printing is rapidly expanding, with the potential for large-scale manufacturing in the near future [1]. Although multi-physics frameworks have been used to simulate the laser sintering process in polymers, accurately predicting the interaction between the laser heat source and the particulate polymer during sintering remains a challenge. Therefore, there is a critical need to develop more advanced rheological contact models and gain new insights into the underlying mechanisms of the process.

To accurately describe the LS process of a particulate polymer and the laser interaction, the flow behaviour of the material during contact (contact rheology) is a relevant characteristic to be explored as a function of the energy absorbed from the incident beam. An increasing number of studies have investigated sintering and heat transfer of polymer powders [2–5], either using the discrete element method (DEM) [6–9] or the finite element method (FEM) [10], and by including the laser beam as a Gaussian heat source function [11–13]. Nonetheless, these descriptions of polymer sintering present a discrepancy compared to

A. H. Nijkamp, H. Cheng, S. Luding and T. Weinhart have contributed equally to this work.

✉ J. E. Alvarez
j.e.alvareznaranjo@utwente.nl

✉ H. Cheng
h.cheng@utwente.nl

✉ T. Weinhart
t.weinhart@utwente.nl

A. H. Nijkamp
a.h.nijkamp@alumnus.utwente.nl

S. Luding
s.luding@utwente.nl

[1] Department of Thermal and Fluid engineering, Faculty of Engineering Technology, University of Twente, Drienerlolaan 5, 7522 NB Enschede, Overijssel, The Netherlands

[2] Department of Civil Engineering and Management, Faculty of Engineering Technology, University of Twente, Drienerlolaan 5, 7522 NB Enschede, Overijssel, The Netherlands

Published online: 12 February 2024

experimental data due to the transient contact rheology, thermal properties and material degradation state that polymers suffer while flowing and for which the aforementioned descriptions are unable to predict. For instance, Hejmady et al. [14] showed that the sintering kinetics is determined by a complex interplay between the sintering mechanisms caused by the relaxation times of polymers, such as polystyrene, and the time-dependent temperature profile which also affects the polymer flow resistance. Even further, the model implemented to describe the neck growth disagreed with the experimental observations due to the aforementioned events. Polychronopoulos et al. [15] proposed a model for neck growth by assuming planar extensional flow for a Newtonian fluid, which results were compared with experimental data on polymer particles. Even though the predictions showed relatively good agreement on the densification rates, it was less accurate for the neck growth rate itself.

In this investigation, we conduct a numerical study of neck growth in polymer powders during laser sintering. Initially, we include the visco-elasto-plastic discrete element model, proposed by Luding et al [16, 17], into the direct heat transfer model of conduction, convection, and radiation, developed by Peng et al. [18]. This thermo-mechanical model is implemented in MercuryDPM [20], an open-source software package, introducing a novel feature for multi-physical particle simulations.

Subsequently, we propose a new contact model for sintering, based on the work of Lin et al. [19] who proposed that the rate of sintering in viscoelastic particles is driven by at first by adhesive contact forces, then adhesive intersurface forces, and finally surface tension. To ensure the conservation of mass, we extend Lin's sintering model by allowing the particle radius to grow during the sintering process, as proposed by Pokluda et al. [20]. As a consequence, a new model parameter, named fluidity, is introduced to control the flow rate as a function of time and temperature.

Then, we present a novel ray-tracing approach for laser energy absorption. This approach simulates the way light travels inside an overlapping set of particles. Consequently, the energy absorption from a laser beam is defined as a function of particle-particle interpenetration. This function allows for the computation of the temperature increment that particles experience at every time step during the simulations when the laser is active, which is needed to activate the sintering process.

Finally, we calibrate the model parameters using experimental data collected from literature [14, 21]. Our simulations incorporate a novel approach developed by Cheng et al. [22, 23] that recursively infers the probabilistic distribution of a set of parameters based on reported observations related to neck growth and temperature evolution during the laser sintering of PA12 and PS particle pairs.

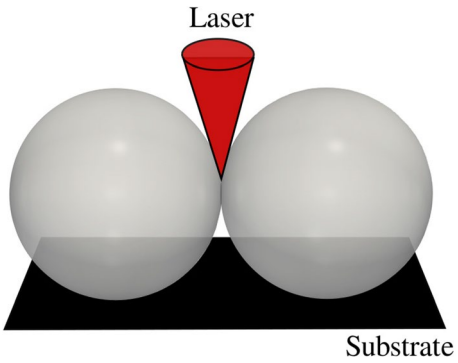


**Fig. 1** Schematic representation of the experimental procedure

**Table 1** Material properties and laser configuration

| Property, symbol - units | PA12 | PS |
|---|---|---|
| Radius, $R_i$ - [$\mu$m] | 125 | 60 |
| Density, $\rho$ - [kg/m$^3$] | 1020 | 1040 |
| Thermal conductivity, $k_{cond}$ - [W/(mK)] | 0.240 | 0.167 |
| Thermal expansion, $\delta_{aT}$ - [1/°C] | $1.0 \times 10^{-4}$ | $1.7 \times 10^{-5}$ |
| Heat capacity, $c_p$ - [J/(kg K)] | 1200 | 1320 |
| Surface tension, $\gamma$ - [mN/m] | 34.3 | 35.6 |
| Young's Modulus, $E$ - [MPa] | 1650 | 1226 |
| Poisson's ratio, $\nu$ - [-] | 0.34 | 0.35 |
| Chamber Temperature, $T_c$ - [°C] | 155 | 53 |
| Pulse duration, $t_L$ - [ms] | 1 | 800 |
| Laser radius $R_L$ - [$\mu$m] | 15 | 20 |
| Laser irradiated energy, $E_{in}$ - [$\mu$J] | 192 | 19–27 |

## 2 Experimental data

Experimental data on laser sintering of PA12 and PS particle pairs were reported by Hejmady et al. [14, 21]. The authors measured the neck growth rate of particle pairs under different conditions and laser set-ups. Thus, several case studies were discussed in detail such as the effect of particle size, heating chamber temperature, laser pulse duration and laser energy. In this work, we have collected the reported information on the effect of laser energy on the neck growth of particle pairs and the temperature evolution of the system during the laser interaction. Figure 1 depicts a schematic illustration of the experimental procedure.

Two particles of similar size are positioned on a substrate within a heating chamber. The interface between the particles is aligned with the laser beam, as well as with the optical focus. A laser pulse is then directed locally at the contact point between the particles, and the neck sintering is captured through optical imaging. Table 1 summarizes

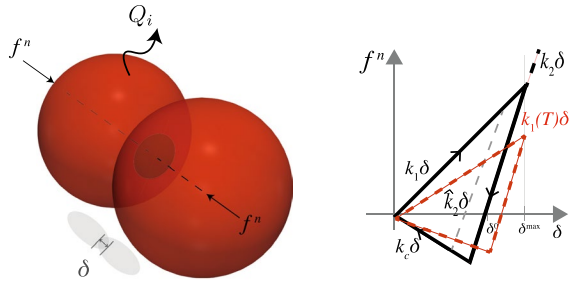


**Fig. 2** (Right) Two particle contact with overlap $\delta$. (Left) Thermo visco-elastoplastic contact law. The contact displacement is related to $\delta$ (overlap) and the normal contact force $f^n$. Right/left-pointing arrows are used to distinguish the forces obtained during the loading and unloading stages, respectively. The dotted line represents the loading stiffness $k_1$ variation according to the increment of temperature $T$, $k_2$ is the unloading stiffness, $k_c$ is the cohesive stiffness

the properties of the polymers and laser set-up used in the experimental configuration [14, 21].

The pulse duration and laser irradiated energy in both experiments are different, as indicated in Table 1. In the case of PA12 particles, sintering occurred around the melting point ($T_{\text{melt}} \sim 180$ °C), predominantly during the cooling stage. This configuration closely approximates the thermal evolution of a real 3D printing process. Conversely, PS particles were sintered slightly above the glass temperature ($T_g \sim 62$ °C, $T_{\text{melt}} \sim 100$ °C) and during the pulse duration, while the laser was still active. This configuration facilitated a slower sintering process, while still imparting sufficient energy for particle pairs to undergo sintering under the influence of surface tension.

## 3 Methods

This section describes the discrete element model (DEM) used to simulate the sintering of particles by a laser beam, which is based on momentum and heat balance [16, 18], implemented in MercuryDPM [24].

### 3.1 DEM and heat transfer

To model heat transfer using a DEM framework, the descriptions of conduction, convection and radiation proposed by Peng et al. [18] are utilised. The particles physically need to come into contact, see Fig. 2 (left). Conversion of heat and balance are employed to estimate the change of temperature of a particle $i$ of radius $R_i$, with the assumption of no temperature gradient within a particle, verified in Sect. 4.2.

In the following, we will assume that the laser heat is applied instantaneously, and thus only affect the initial conditions. Therefore, we assume that there is no heat source and the evolution of particle temperature is described by

$$m_i c_{p,i} \frac{\mathrm{d}T_i}{\partial t} + \sum_{j=1}^{n} k_{i,cond}(T_j - T_i)\frac{a_{ij}}{l_{ij}} = Q_{i,conv} + Q_{i,rad}, \tag{1}$$

where $m_i$ is the particle mass, $c_{p,i}$ is the heat of material, and $T_i$, $T_j$ are the temperatures of particles $i$, $j$, respectively. $k_{cond}$ is the conductivity of material, $l_{ij}$ the distance between the centers of particles, $Q_i$ represent the external heat fluxes associated to particle $i$ by convection ($Q_{i,conv}$) and radiation ($Q_{i,rad}$) with units [W], and $n$ is the number of interacting neighbors of particle $i$. The area of heat transmission, $a_{ij}$, can be correlated to the overlap $\delta_{ij} = (R_i + R_j) - (\mathbf{r}_i - \mathbf{r}_j) \cdot \mathbf{n}$, where $\mathbf{r}_i$ is the position of particle $i$ with unit vector $\mathbf{n} = (\mathbf{r}_i - \mathbf{r}_j)/|\mathbf{r}_i - \mathbf{r}_j|$, and the effective particle radius $R_{ij} = R_i R_j/(R_i + R_j)$, so that:

$$a_{ij} \simeq 2\pi R_{ij}\delta_{ij}, \tag{2}$$

for $\delta_{ij} \ll R_{ij}$.

The convective heat transfer can be expressed as:

$$Q_{i,conv} = k_{i,conv} A_i (T_f - T_i), \tag{3}$$

where $A_i$ is the surface area available on particle $i$, with $T_i$, $k_{i,conv}$ is the convective heat transfer coefficient, $T_f$ is the surrounding temperature, and $Q_{i,conv}$ represents the heat flux of particle $i$ with the environment.

The radiative heat transfer is expressed as:

$$Q_{i,rad} = \sigma \varepsilon A_i (T_{i,local}^4 - T_i^4), \tag{4}$$

where $\sigma = 5.67 \times 10^{-8}$ W/m$^2$K$^4$ is the Stefan-Boltzmann constant, $\varepsilon$ represents the emissivity with dimensionless quantity, and $T_{i,local}$ is the temperature of the environment.

Subsequently, the motion of particles is solved based on Newton's equations of motion, where the corresponding translational and rotational degrees of freedoms are simultaneously updated with Eq. (1), which are expressed as,

$$m_i \ddot{r}_i = m_i g + \sum_j f_{ij}^n \tag{5}$$

$$I_i \ddot{\theta}_i = \sum_j (r_{ij} \times f_{ij}^n), \tag{6}$$

where $\ddot{r}_i$ is translational acceleration, $m_i$ mass of the particle $i$, $g$ acceleration due to gravity, $f_{ij}^n$ force at contact with particles. $\ddot{\theta}_i$ is angular acceleration, $r_{ij}$ the branch vector directed from the center of particle $i$ to the contact point with particle $j$, and $I_i$ is the mass moment of inertia of particle $i$.

For the inter-particle collision, the temperature dependence contact model proposed by Luding [16] is used, see Fig. 2, (right). The normal force $f_{ij}^n$ describes the interaction as:

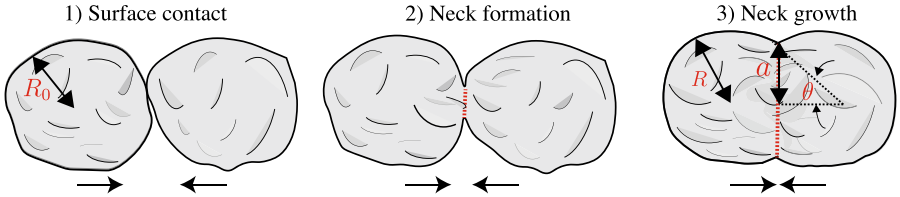


**Fig. 3** Schematic illustration of the polymer sintering process. (1) Surface contact. (2) Neck formation. (3) Neck growth. $R$ represents the particle radius, $a$ is the contact radius, $\theta$ is the angle of intersection

$$f_{ij}^{n} = \left\{ \begin{array}{ll} k_1(T)\delta_{ij} & \text{if } \delta_{ij} > \delta_{ij}^{\max} \\ k_2(\delta_{ij} - \delta_{ij}^{0}) & \text{if } \delta_{ij}^{\min} < \delta_{ij} \leq \delta_{ij}^{\max} \\ -k_c\delta_{ij} & \text{if } 0 < \delta_{ij} \leq \delta_{ij}^{min} \end{array} \right\} - f_{ij}^{a} - \eta^{n} v_{ij}^{n}. \quad (7)$$

The computation of the repulsive visco-elastoplastic forces $f_{ij}^{n}$ during sintering is governed by the loading stiffness $k_1(T)$. It decreases as $T$ approaches the melting point of a material, and therefore, the material can deform significantly so that the contact area becomes larger at the contact. The dependency of $k_1$ on $T$ may be described as:

$$k_1(T) = \frac{k_1}{2}\left[1 + \tanh\left(\frac{T_{\text{melt}} - T}{T_{\text{var}}}\right)\right], \quad (8)$$

where $T_{\text{var}}$ defines the range of temperatures in which the melting takes place. In the transition regime where $\mid T_{\text{melt}} - T \mid / T_{\text{var}}$, the particles are significantly softer than in the cold limit $T_{\text{melt}} - T \gg T_{\text{var}}$. Subsequently, the unloading process follows the slope of $\hat{k}_2$, which varies between $k_1(T)$ at a given temperature and a constant $k_2$, depending on the plastic deformation at zero force $\delta_{ij}^{0}$. Note that $k_2$ is not changed directly when $T$ increases. For overlaps smaller than $\delta_{ij}^{\max}$, the unloading stiffness is interpolated linearly between $k_2$ and $k_1(T)$ as:

$$\hat{k}_2 = \left\{ \begin{array}{ll} k_1(T) + (k_2 - k_1(T))\frac{\delta_{ij}^{\max}}{\phi_f R_{ij}} & \text{if } \delta_{ij}^{\max} < 2\phi_f R_{ij} \\ k_2 & \text{if } \delta_{ij} \geq \delta_{ij}^{\max} \end{array} \right\}, \quad (9)$$

where $\phi_f = \sqrt[3]{2}$ and $R_{ij}$ represents the effective particle radius. After the contact force becomes negative, for $\delta_{ij} < \delta_{ij}^{0}$, the model introduces a cohesive force limited by the cohesion stiffness $k_c$.

The additional adhesive force $f_{ij}^{a}$ is assumed constant in Eq. (7). In the case of collisions of particles and large deformations, dissipation occurs due to the hysteretic nature of the force-law described by a viscous, dissipative, velocity-dependent force $\eta^{n} v_{ij}^{n}$, with $\eta^{n}$ as the viscous dissipation coefficient. This coefficient is related to the restitution coefficient $e$ as $\eta^{n} = \sqrt{2mk_1}/(\sqrt{\pi} + \sqrt{\log e})\log e$, and therefore, this force-displacement model depends only on particle mass, not relative velocity.[1]

Finally, if particles are heated their volume increase so that their density decrease. Thus, we assume that the particle radius changes in linear approximation as

$$R_i(T) = R_i(T_{\text{melt}})[1 + \delta a_T(T_{\text{melt}} - T)], \quad (10)$$

with the relative change of the radius per unit temperature $\delta a_T$.

### 3.2 Contact rheological model for polymer sintering

The sinter bonding of polymer particles occurs between their glass transition and melting points, resulting in the formation of necks that reduce surface area and lower surface energy. The necks grow through atomic-level transport of polymer chains along grain boundaries and bulk grain. Various mechanisms influence sintering, with visco-elastic deformation and viscous flow being the most dominant for polymer particles [19, 25, 26]. Figure 3 illustrates the stages of a polymer sintering process.

The mechanisms for the polymer sintering process involve three stages: surface contact, neck formation and neck growth. First, the surface contact represents the adhesion stage, in which the particles first attract each other via van der Waals adhesion forces. Second, neck formation occurs while the visco-elastic deformation is balanced by quick intersurface adhesive forces during the material's unrelaxed state. The last stage corresponds to the relaxation of molecular rearrangement, and is related to the action of surface tension in the viscous flow regime. By defining the evolution of contact radius $a_{ij}/R_{ij}$ during the three mentioned stages, it is possible to include each stage into a DEM approach correlating the particle-particle overlap $\delta_{ij}$ during the computation of the normal force $f_{ij}^{n}$, see Eq. (7). Our previous investigation has discussed mathematically $a_{ij}/R_{ij}$ for polymer sintering, and therefore, the reader is referred to [25] for more details. Nonetheless and most important, the latest stage of the process (3) is improved with

[1] This is a particular case by assuming $k_1 = k_2$.

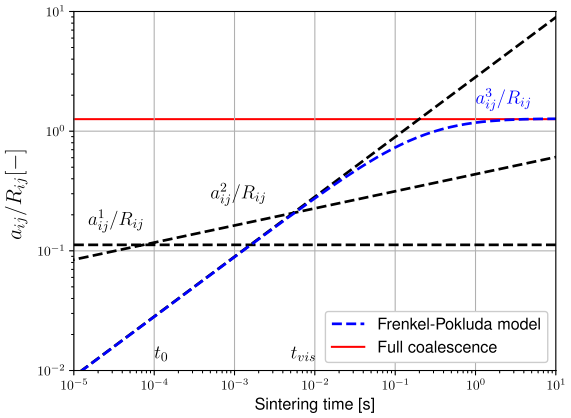


**Fig. 4** Sintering regime map with three mechanisms for flow simulation: (1) adhesive contact, (2) adhesive inter-surface forces, and (3) surface tension. If $t < t_0$, $a^1_{ij}/R_{ij}$ is a constant derived from JKR theory. For intermediate times $t_0 < t < t_{vis}$, a power-law behaviour emerges, $a^2_{ij}/R_{ij} \sim t^{1/7}$, exhibiting only weakly time-dependent growth. For $t > t_{vis}$, Frenkel model $a^3_{ij}/R_{ij} \sim t^{1/2}$ (black dashed line), or Frenkel-Pokluda model $a^3_{ij}/R_{ij} \sim \sin(\theta(t))$ (blue dashed line), indicative of viscous sintering, which results in faster growth

Frenkel-Pokluda model [20], leading to a dependent fluidity $C_1$,[2] a new time and temperature-dependent parameter. Figure 4 illustrates the sintering regime map, remarkably controlled by only one parameter $C_1$, at the last stage.

In stage 1, the non-dimensional neck radius $a^1_{ij}/R_{ij}$ was derived by Johnson, Kendall, and Roberts [27] at very short times ($t \ll t_0$) for the equilibrium deformation of two elastic bodies under the influence of surface tension. Thus, the elastic repulsion using the Hertz equation is balanced by the adhesive traction of the particles, giving as:

$$\frac{a^1_{ij}}{R_{ij}} = \left(\frac{9\pi(1-\nu^2)\gamma}{ER_{ij}}\right)^{1/3}, \tag{11}$$

where $\gamma$ is the surface tension, $\nu$ the Poisson's ratio, and $E$ the Young's modulus. Within this adhesive stage, the contact radius is not time-dependent due to the time-invariant modulus, which is that of a glassy solid, and a very rapid swing-in period, which is neglected.

In stage 2, for intermediate times in the interval $t_0 < t < t_{vis}$, the second stage of neck growth is due to visco-elastic deformation of the particles balanced by inter-surface adhesive forces acting in the region around the contact area, the growth of contact radius $a^2_{ij}$ is predicted to be:

$$\frac{a^2_{ij}}{R_{ij}} = \left(\frac{63\pi^3}{16}\right)^{1/7}\left(\frac{\delta_c}{R_{ij}}\right)^{2/7}\left(\frac{2C_1\gamma t}{R_{ij}}\right)^{1/7}, \tag{12}$$

where the separation distance $\delta_c$ is specified to ensure the work of adhesion, defined as the range of the adhesive force, and $t$ is time. For this, two main phenomena required being involved while the visco-elastic particles are bonding: creep compliance and stress relaxation. First, creep $C(t)$ quantifies the capacity of a material to flow in response to a sudden applied stress. Second, stress relaxation indicates the moment at which a visco-elastic material relieves stress under strain. Therefore, the strain rate $\epsilon$ is a function of time under instantaneous application of constant stress $\sigma$, expressed in a non-Hookean fashion as:

$$\epsilon(t) = C(t)\sigma. \tag{13}$$

The contact creep compliance is a useful metric that quantifies a unique mechanical response, defined by

$$C(t) = C_0 + C_1 t^m, \tag{14}$$

where $C_0 = (1-\nu^2)/E$ represents the instantaneous compliance, $C_1$ is a material property, called "fluidity" in our work, and $0 < m < 1$.

In stage 3, the growth of the contact radius $a^3_{ij}$ was initially derived by Frenkel [28], showing that for a Newtonian fluid, the evolution of $a^3_{ij}$ may fulfil a scaling law. It is by equating the rate of surface tension work to the viscous flow energy dissipation rate, giving

$$\frac{a^3_{ij}}{R_{ij}} = \left(\frac{8\gamma C_1 t}{R_{ij}}\right)^{1/2}. \tag{15}$$

Frenkel's model has been used to describe the sintering rate on the early stage of the process. In contrast, Pokluda et al. [20] developed a sintering model considering the variation of the particle radius with time, and for which this investigation is used. For that, the relation for the particle radius $R_{ij}(t)$ versus the sintering angle $\theta(t)$ can be obtained from the conservation of mass with the assumption of a constant density as:

$$R_{ij} = R_0\left[\frac{4}{(1+\cos(\theta))^2(2-\cos(\theta))}\right]^{1/3}, \tag{16}$$

where $R_0$ is the initial particle radius, see Fig. 3. Thereby, the work of surface tension $W_s$ is defined as:

$$W_s = -\Gamma\frac{dS}{dt} \tag{17}$$

where $S = 4\pi R^2_{ij}(1+cos(\theta))$. Thus, the work of surface tension depends solely on the rate of surface reduction rather than on the surface curvature. Considering the variation of

[2] Fluidity, $C_1$, is the term adopted to describe the non-opposition to flow.

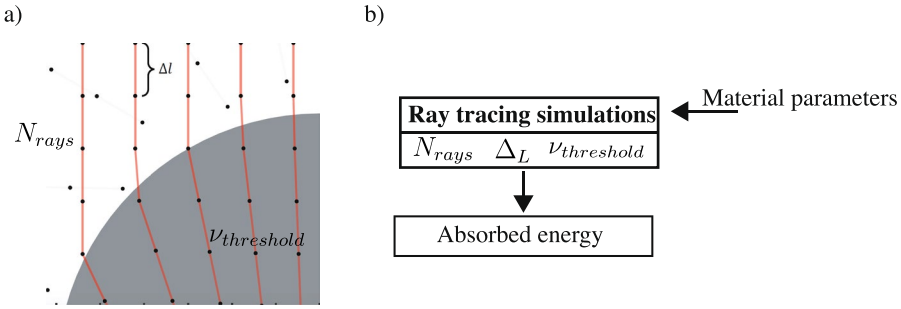


**Fig. 5** **a** A laser beam represented by several light rays interacts with a particle, causing the rays to be split into reflected and refracted rays. **b** The ray tracing simulation is set with material, laser parameters and model configuration such as the number of rays $N_{rays}$, step size $\Delta l$, dissipation threshold $\nu_{thershold}$

the particle radius with time, the expression of the work of surface tension becomes:

$$W_s = \Gamma \frac{8\pi R_0^2 2^{1/3} \cos(\theta)\sin(\theta)}{(1+\cos(\theta))^{4/3}(2-\cos(\theta))^{5/3}} \frac{d\theta}{dt} \tag{18}$$

The work of viscous forces, assuming flow field as extensional and for Newtonian fluid, can be expressed as:

$$W_\nu = 32\pi R_0^3 \eta \dot{\epsilon}^2 \tag{19}$$

where $\dot{\epsilon}$ is the strain rate, assumed to be constant throughout the complete domain [20], and was approximated by

$$-2\dot{\epsilon} \approx \frac{d(R_{ij}\cos(\theta))/dt}{R_{ij}} \tag{20}$$

By equating the work of surface tension to the viscous dissipation, knowing that $\Gamma/\nu = 8C_1\gamma$, Pokluda et al. [20] obtained

$$\frac{d\theta}{dt} = \frac{8\gamma C_1}{R_0} \frac{2^{-5/3}\cos(\theta)\sin(\theta)[2-\cos(\theta)]^{1/3}}{(1-\cos(\theta))(2-cos(\theta))^{1/3}}. \tag{21}$$

Considering that $\theta > 0$ and applying the initial condition $\theta(0) = \theta_0 = 0$, the corresponding Frenkel model is obtained.

$$\theta(t) = \left(\frac{8\gamma C_1 t}{R_0}\right)^{1/2}. \tag{22}$$

Once the solution for the evolution of the sintering angle with time is obtained, the evolution with time is derived [20],

$$\frac{a_{ij}^3}{R_{ij}} = \sin(\theta), \tag{23}$$

$$\frac{a_{ij}^3}{R_0} = \sin(\theta)\left[\frac{4}{(1+\cos(\theta))^2(2-\cos(\theta))}\right]^{1/3}. \tag{24}$$

Assuming that the surface tension $\gamma$ is constant in Eq. (22), fluidity $C_1$ can be controlled as a function of temperature to decrease the degree of sintering.

To include $a_{ij}^1, a_{ij}^2$, and $a_{ij}^3$ in the contact description (Eq.(7)), we compute the rate of the plastic overlap $\dot{\delta}_{ij}^0$. Knowing that the overlap between the particles nearly equals the plastic overlap, $\delta_{ij} \approx \delta_{ij}^0$ for stiff particles $(k_1 \gg (f_{ij}^n + f_{ij}^a)/R_{ij})$, the contact radius may be approximated as $a_{ij}/R_{ij} \approx \sqrt{\delta_{ij}/R_{ij}}$ (small overlaps $\delta_{ij}^0 \ll R_{ij}$). It can be controlled by setting the growth rate $\dot{\delta}_{ij}^0$ according to Eqs. (11), (12), and (24).

### 3.3 Ray tracing approach for laser energy absorption

An absorption model is needed to describe the interaction of a laser source and the particles. According to the Beer-Lambert law, the decrease of attenuation of the light intensity while propagating inside a material can be described as:

$$I(x) = I_0 e^{-\mu x}, \tag{25}$$

where $I_0$ is the initial light intensity, $\mu$ represents the attenuation coefficient of a material, $x$ is the path. Yaagoubi et al. [29] presented a model to describe the laser as a set of rays, where each ray is traced along the path that it follows, with step size $\Delta l$ and by which particles it is absorbed, until it is completely absorbed or has left the material. However, the equation only applies to 2D cases. In our study, the 3D equation to determine the starting intensity of each ray is based on a Gaussian laser profile, scaled such that the total intensity of all rays equals 1 and set to:

$$I_0\left(d, R_{laser}, N_{ray}\right) = \frac{2}{N_{ray}\left(1-\frac{1}{e^2}\right)} e^{\frac{-2d^2}{R_{laser}^2}}, \text{ if } d < R_{laser}, \ 0 \ else, \tag{26}$$

**Table 2** Optical interaction coefficients

| Property, symbol - units | PA12 | PS |
|---|---|---|
| Refraction index, $n$ [-] | 1.525 | 1.5997 |
| Attenuation coefficient, $\mu$ [$m^{-1}$] | 33500.0 | 27400.0 |

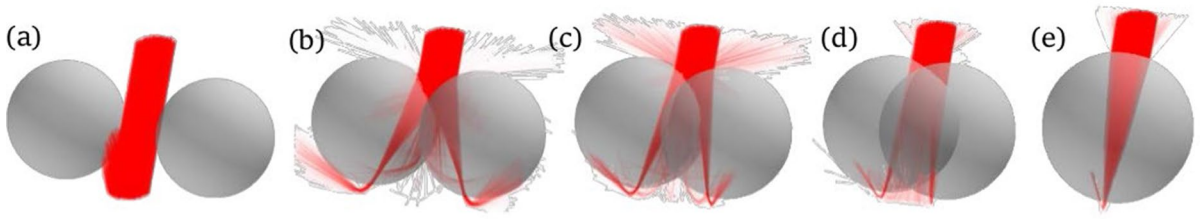


**Fig. 6** Ray tracing simulations for PA12 particle pairs, depicting incident beam rays onto two spherical particles at different overlaps: **a** $\delta_{ij}/2R_{ij} = -1/3$, **b** $\delta_{ij}/2R_{ij} = 1/20$, **c** $\delta_{ij}/2R_{ij} = 1/3$, **d** $\delta_{ij}/2R_{ij} = 1/2$, **e** $\delta_{ij}/2R_{ij} = 1$

where $N_{ray}$ represents the number of rays, $d$ is the distance from the laser centre perpendicular to the propagation direction, and $R_{laser}$ is laser radius. The implemented ray tracing model, whose accuracy depends on the number of rays, step size $\Delta l$, and dissipation threshold $v_{threshold}$, is documented and can be downloaded via Github.[3] Figure 5 illustrates the approach, implemented in MercuryDPM.

Since each simulation in the ray tracing approach is performed for a single time step, the simulations provide the amount of energy that particles absorb in each time step using the momentum of particle-particle interpenetration. This allows for the computation of the heating rate of a certain particle, which is given by,

$$\frac{\Delta T}{\Delta t} = \frac{E_{in} e_{abs}}{m c_p}, \tag{27}$$

where $E_{in}$ is the total irradiated laser energy, $e_{abs}$ the portion of absorbed energy out of the total incoming energy, $\Delta t$ the time step, $m$ and $c_p$ are mass and heat capacity of the particle.

## 4 Results and discussion

This section presents a computational analysis of the contact rheology of visco-elastic powders during laser sintering, using the experimental data on PA12 and PS discussed in Sect. 2, and earlier reported in [25]. The analysis begins with ray tracing simulations to determine the amount of energy absorbed by the particles when irradiated by the laser beam. Next, the neck growth and the calibration procedure used.

### 4.1 Absorption analysis

To determine the portion of energy absorbed ($e_{abs}$) by particles while a laser beam irradiates the surface, ray tracing simulations are conducted (see Sect. 3.3). First, the refraction index and the attenuation coefficient of PA12 and PS are extracted from the literature [21, 30], as summarized in Table 2.

It is noticed that PA12 presents a larger attenuation coefficient compared to PS, i.e. the incident energy beam becomes more attenuated as it passes through the material, and therefore, more energy would be absorbed by this polymer per length. Subsequently, the laser spot radius is set to 15 $\mu$m and 20 $\mu$m for PA12 and PS, respectively, according to the experimental data (Table 1). The laser beam has an angle of incidence of 60° related to the particle bed surface normal. It is also assumed that the bed perfectly reflects the light rays and the laser impacts precisely at the contact point of the two adjacent particles. The temperature is homogeneously diffused inside the particles as suggested by Balemans et al. [11]. Finally, the ray tracing discretization parameters are set to $N_{rays} = 10000$, step size $\Delta l = 10\%$, and a dissipation threshold $v_{thresh} = 1\%$. The parameters were tested and adjusted until the simulations converge with less than 1% of variation. The ray tracing simulation for a PA12 particle pair is illustrated in Fig. 6.

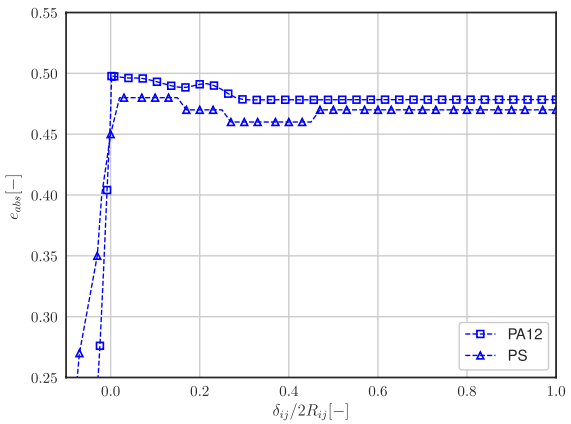


**Fig. 7** The absorbed energy portion of a particle in pair, as a function of overlap $\delta_{ij}/2R_{ij}$, where contacts are positive. Squared shapes represent the results using PA12 properties while triangle shapes indicate the computations using PS properties

[3] https://github.com/BertNijkamp/Laser-Beam-Absorption.

Figure 6 shows the simulation of ray tracing while particle pairs are overlapping from $\delta_{ij}/2R_{ij} = -1/3$ to $\delta_{ij}/2R_{ij} = 1.0$, being $\delta_{ij}/2R_{ij}$ the relative overlap if positive. The simulation shows differences in light reflection when the relative overlap is varied. For instance, a relatively big portion of the energy is reflected away from the top at $\delta_{ij}/2R_{ij} = 1/20$, and the light rays are more converging to each other when $\delta_{ij}/2R_{ij} \approx 1$. It is evidenced that the energy absorbed by a polymer not only depends on the shape on which the laser impacts but also on the amount of overlap caused by sintering. Subsequently, the absorbed energy portion $e_{abs}$ can be defined as a function of particle overlap $\delta_{ij}/2R_{ij}$, as depicted in Fig. 7.

Figure 7 shows that PA12 absorbs slightly more energy ($2 \sim 3\%$), as it attenuates stronger compared to PS. The amount of absorbed energy for both materials is higher when the particles are in contact $\delta_{ij}/R_{ij} \geq 0$, as the area to irradiate increases, and therefore, the particles absorb more energy. With increasing distance between the particles $\delta_{ij} < 0$, less incident bean rays irradiate the particles, as depicted in Fig. 6. Furthermore, the two systems absorb the incident energy differently. For PA12, the highest absorption is identified at the initial contact $\delta_{ij}/2R_{ij} = 0$, and it decreases with particle overlap up to 30%, the moment at which the absorbed energy is constant, losing about 5% of the initial laser irradiated energy. For PS, the highest absorption is at the initial contact with $1-3\%$ of loss compared to the incident energy, it fluctuates, until reaching its asymtotic limit at $> 45\%$ of the overlap, leading to a 7% loss of total energy. The fluctuating behaviour in the case of PS material is the consequence of the smaller particle radius (60 $\mu$m), the lower attenuation coefficient, and also due to internal reflections of the beam inside the particle. It is relevant to mention that the curvature effect at the particle contact does not significantly affect light propagation. Since our ray tracing simulations are conducted for equal sized spheres, the rays may bend uniformly. Future studies can focus on different particle sizes and the consequence bending of light.

The absorbed energy curves presented in Fig. 7, are set into MercuryDPM as a simple polynomial fit, $e_{abs}(\delta_{ij}/2R_{ij})$. Due to the usage of these fitting, the sintering simulation in MercuryDPM does not need to perform a ray tracing simulation, simply the polynomial equation can be used to calculate the relative amount of absorbed energy per time step, decreasing the computational cost. Once the sintering simulation starts, the temperature of the system is updated every time step according to the laser irradiated energy $E_{in}$, pulse duration $t_L$ (reported in Table 1) and the modes of heat transfer (conduction, convection and radiation), see Eq. (27).

## 4.2 Neck growth contact rheology

Laser sintering of powders is a multi-physics process that involves three different time scales. First, the time scale from the laser energy source, in which the laser is active. Here, we model the absorption process by the ray tracing approach, which assumed the absorption to occur instantaneously. Secondly, the time scale of heat diffusion, which is described throughout particle contacts using DEM for heat transfer problems. We also assume this process acts instantaneously and attributes an uniform temperature within each particle. Thirdly, the time scale from the neck formation, which is addressed by the current sintering regime map (Fig. 4). The later stage depends on the contact rheology of the material, and therefore it is strictly necessary to be defined as evidenced by experimental data [14, 21, 31].

The assumption of the uniform temperature inside each particle applies to all simulations. To determine the validity of this assumption, the thermal resistance of a polymer powder can be analysed based on the Biot number (Bi) [32, 33], being estimated as:

$$\mathrm{Bi} = \frac{hL_c}{k_{cond}} = \frac{h(R/3)}{k_{cond}}, \tag{28}$$

where $h$ is the heat transfer coefficient, $L_c$ is the characteristic length scale which is defined as volume/surface area, and $R$ is the particle radius. $k_{cond}$ represents the thermal conductivity of the particle. For the case of PA12 and PS particles, $\mathrm{B_i} \ll 0.1$, which indicates that the intraparticle heat transfer resistance is small compared to the external resistance around the particle [18]. In other words, the interior of the particles can be considered to be at a nearly uniform temperature.

Subsequently, to calibrate the contact rheology of PA12 and PS for sintering simulations, the open-source package GrainLearning [22] is utilised. It finds the most likely set of model parameters that reproduce the experimental data, based on constrained conditional probability distributions. The calibration package GrainLearning is a Bayesian calibration tool for estimating micro-parameter uncertainties in mechanical models. It uses the recursive Bayes' rule to quantify the evolution of the probability distribution of parameters over data history. The coupled implementation with MercuryDPM is illustrated in Fig. 8.

Using the experimental data on *the evolution of the neck growth* and *temperature evolution* during laser sintering, reported by Hejmady et al. [14, 21], our DEM model requires the calibration of fluidity $C_1$, surface tension $\gamma$, loading stiffness $k_1$, thermal convectivity $k_{conv}$ and emissivity $\varepsilon$. For this, an initial parameter space is defined as reported in Table 3.

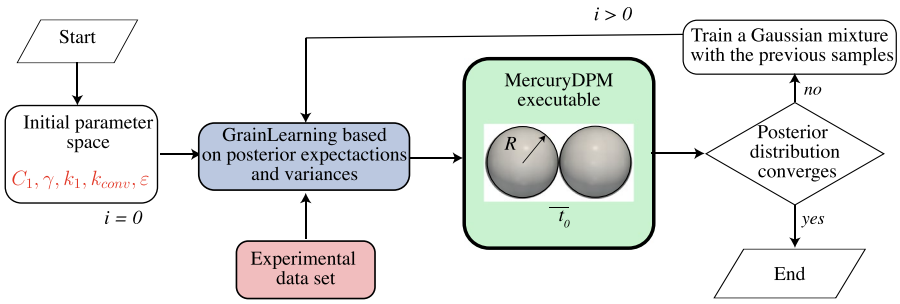


**Fig. 8** Flowchart illustrating the iterative coupled implementation using MercuryDPM and GrainLearning. The parameter space is initially set at iteration $i = 0$ and progressively updated until convergence is achieved

**Table 3** Parameter space

| $C_1$ - [1/(Pa s)] | $\gamma$ - [N/m] | $k_1$ - [N/m] | $k_{conv}$ - [W/(mK)] | $\varepsilon$ [-] |
|---|---|---|---|---|
| 0.001 – 0.1 | 0.01 – 0.05 | 0.0001 – 0.003 | 100 – 1000 | 0.1 – 1.0 |

**Table 4** System parameters

| $k_2$ - [N/m] | $k_c$ - [N/m] | $\delta_c$ - [m$^{-1}$] | $e$ - | $\phi$ [-] |
|---|---|---|---|---|
| 5.0 $k_1$ | 2.0 $k_1$ | 1.0/4.0$R$ | 0.15 | $\sqrt[3]{4}$ |

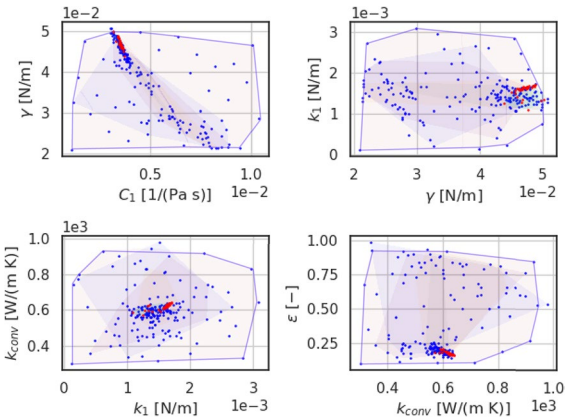


**Fig. 9** Calibration of model parameters for sintering simulations of PA12 particle pairs. Layers indicate the space of the parametric sample at every iteration, being the first layer of the initial parametric space. Blue dots represent the sample points, which progressively converge to a narrowed area. Red dots represent the last estimation of the parameters at the last iteration

The remaining contact parameters are summarized in Table 4 [16, 34]

To simulate the visco-elastic sintering of polymer powders, a pair of 3D spheres of equal diameter is placed next to each other with non-zero overlap between them, as visualized in Fig. 8. The particles are set just in contact at time $t_0$; the gravitational force is neglected. A small adhesive force $f^a = k_1 \delta_a$ is set to the particles to start the motion, where $\delta_a = 1.0$ mm. The range of softening is $T_{\text{var}} = 10$ °C with respect to the melting temperature of the material. Six iterations have been defined for the calibration procedure with eighty samples in each iteration for both PA12 and PS models. The normalized covariance parameter at the first iteration is set to 0.7, resulting in an effective sample size of the Bayesian calibration larger than 20%. Figure 9 shows the iterative calibration procedure for the PA12 model.

The illustration of the re-sampling process presented in Fig. 9 depicts the posterior modes localized progressively after each iteration. The agreement of the posterior expectations before and after one iteration of Bayesian filtering is adopted as the convergence criterion. The posterior expectation of each micro-parameter converges after the fifth iteration. Note that if the initial guesses for the model parameters are not able to capture at least one posterior distribution, the re-sampling scheme could explore outside the parameter ranges specified at the first iteration. The key to iterative Bayesian filtering is the ability to re-sample from a proposal density, that is, the posterior distribution or modes obtained from the previous iteration, for the following iteration. Over iterations, the proposal density is progressively localised near the posterior modes. Table 5 summarizes the calibrated parameters. Consequently, the DEM results are reported.

**Table 5** Calibrated parameters

| Property - units | PA12 | PS | | | | |
|---|---|---|---|---|---|---|
| Irradiated energy, $E_{in}$ - [$\mu$J] | 192.0 | 19.0 | 21.0 | 23.0 | 25.0 | 27.0 |
| $C_1$ - [1/(Pa s)] | 3.41 | 0.03 | 1.92 | 7.36 | 21.51 | 72.8 |
| $\gamma$ - [mN/m] | 48.56 | 50.09 | 42.42 | 42.19 | 25.72 | 24.71 |
| $k_1$ - [mN/m] | 1.67 | 0.11 | 0.11 | 0.12 | 0.12 | 0.148 |
| $k_{conv}$ - [W/(mK)] | 635.73 | 304.10 | 334.4 | 301.11 | 309.2 | 304.74 |
| $\varepsilon$ [-] | 0.164 | 0.21 | 0.275 | 0.76 | 0.805 | 0.814 |

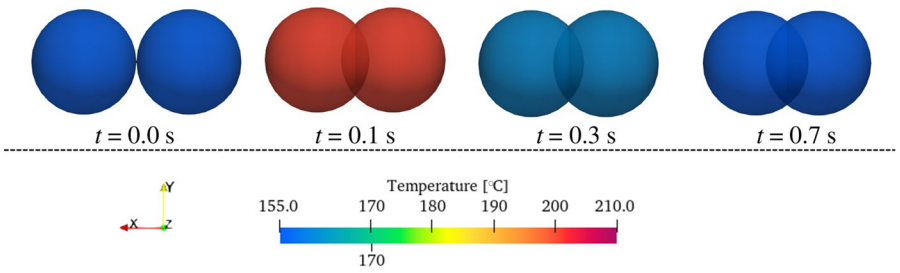


**Fig. 10** Image sequence of sintering PA12 particles of radii $R_i = 125\ \mu$m. Temperature evolution is recorded by the colour change from the first contact at $t = 0.0$ s to $t = 0.7$ s

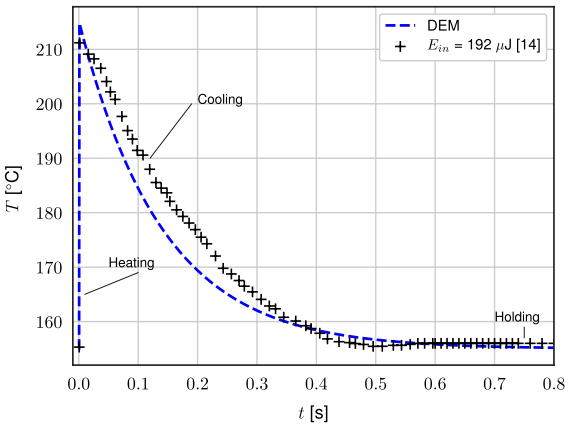


**Fig. 11** Temperature evolution while sintering PA12 particle pairs with $E_{in} = 192\ \mu$J. Initial temperature is set to $T_0 = 155$ °C. Cross markers correspond to the experimental data extracted from [14], while the dashed line is the DEM simulation results

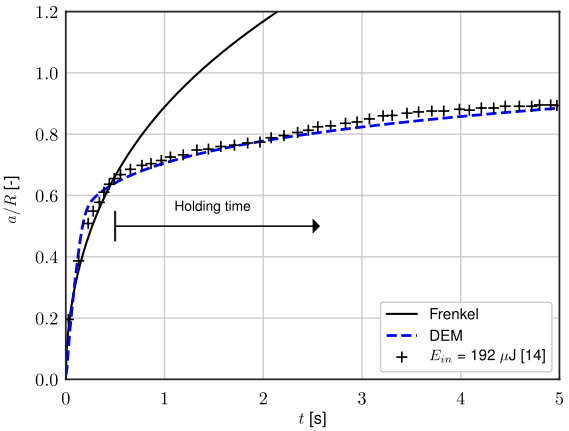


**Fig. 12** Neck growth of PA12 particle pairs. The dashed line corresponds to a calibrated DEM simulation, the solid line describes the modified Frenkel prediction using $\mu = 270$ Pa s, and crosses are the experimental data [14]

It is noticed from Table 5 that surface tension corresponds to the expected ranges of calibration [14], and it increases according to lower irradiated energies, indicating that the material opposes the flowability. Figure 10 presents the calibrated simulation of PA12 particle pairs at different snapshots and temperature evolution.

The simulation result of the temperature evolution on PA12 particles is presented in Fig. 11.

Three stages are indicated during thermal evolution. The heating stage, which increments quickly until the end of the pulse duration at $t = 0.01$ s. Then, the cooling stage starts from the maximum absorbed energy and decays exponentially to the initial or chamber temperature at 0.6 s. It happens because once the particle absorbs the incoming energy and the laser is switched off, the dissipation by radiation and convection reduces the temperature of the system until it reaches the initial conditions. The maximum temperature distributed within the particles when the laser impacts the surface is around 5% of loss over the irradiated energy. According to the characteristic time for heat diffusion $t_{diff}$ [32], heat diffuses completely through the particles at $t = 0.4$ s, the moment at which the particles are to achieve the temperature of the holding period as indicated by the experimental data. It is shown that the heat transfer model describes the experimental data relatively well, with only a slightly faster cooling than expected during the cooling stage. While our simulation effectively captures the maximum temperature produced by an activated laser beam, the cooling rate reveals a dissipation of heat through convection and conduction at a faster rate, with approximately a 2.5% error compared to experimental data. To enhance the precision of our heat transfer model, several refinements may be proposed. These include incorporating additional mechanisms such as conduction through the surrounding fluid, convection between fluid and solid particles, convection between fluid and wall, radiation between the solid particles and between fluid and solid particles. Integrating these refinements in future studies aim to provide a more comprehensive and accurate representation of the heat transfer dynamics using our model.

Subsequently, the neck growth of particle pairs (Fig. 10) is computed and the results presented in Fig. 12.

According to the experimental set-up, the sintering of PA12 particle pairs occurs principally during the holding stage ($t > 0.6$ s) after the temperature reaches the initial condition, as indicated by the horizontal arrow in Fig. 12. This is the consequence of letting the system remain at a temperature above the glass point, which allows the material

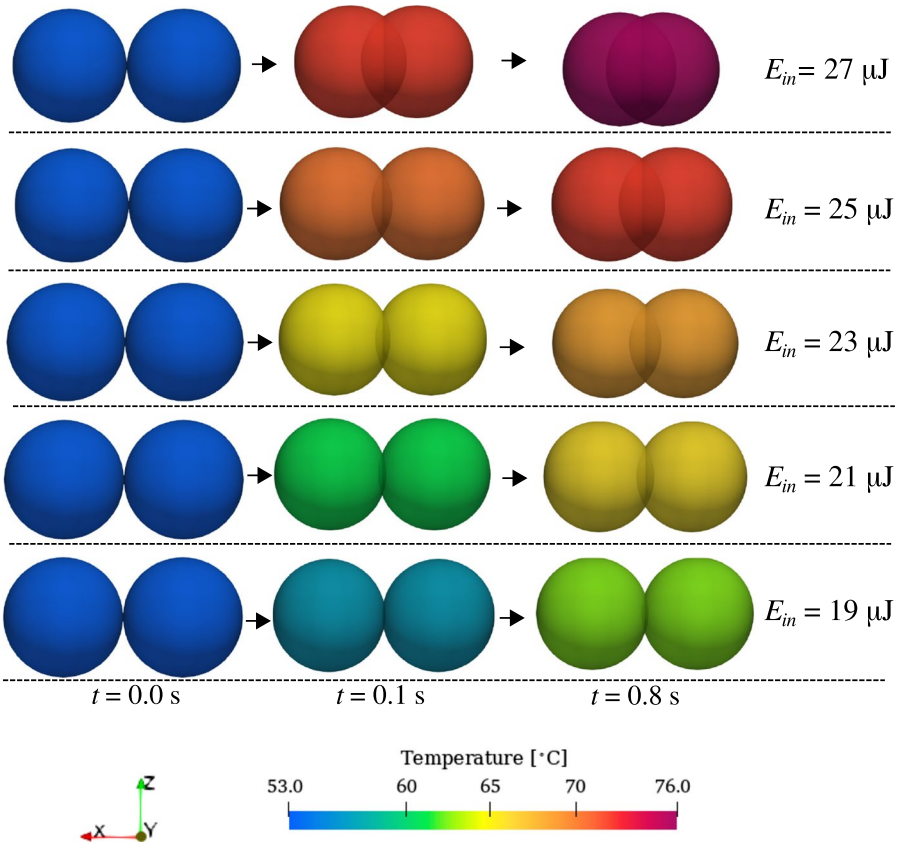


**Fig. 13** Imagine sequences of sintering PS particles of radii $R_i = 60$ $\mu$m. The temperature evolution is indicated by the colour change from the first contact at $t = 0.0$ s to $t = 0.8$ s, for different overlaps $\delta_{ij}$

**Table 6** Comparison between laser irradiated energy and energy portion absorbed $e_{abs}$ by particle pairs using the current ray tracing model

| $E_{in}$ [$\mu$J] | 27.0 | 25.0 | 23.0 | 21.0 | 19.0 |
|---|---|---|---|---|---|
| $e_{abs}E_{in}$ [$\mu$J] | 25.3 | 23.4 | 21.5 | 19.5 | 17.6 |
| $e_{abs}$ [%] | 93.7 | 93.6 | 93.4 | 92.9 | 92.6 |

to permanently deform under the influence of visco-plastic forces.

As indicated in Fig. 12, dynamics indeed initiate before the diffusion time, particularly evident in the experimental case of PA12 where particles undergo sintering more rapidly than the complete heat diffusion throughout the entire volume. It is important to note that while this limitation exists in our current Discrete Element Method (DEM) model, attempting to resolve temperature gradients inside particles would require a spatial discretisation within each particle, significantly increasing the computational complexity and falling beyond the scope of our present investigation. Therefore, for the sake of model simplification, we assume that no temperature gradient exists inside the particles.

Frenkel's model has been usually employed in the literature to describe sintering of particle pairs [28, 35, 36]. However, the model is only valid for the initial stage of the process as evidenced in Fig. 12, being fitted with a viscosity

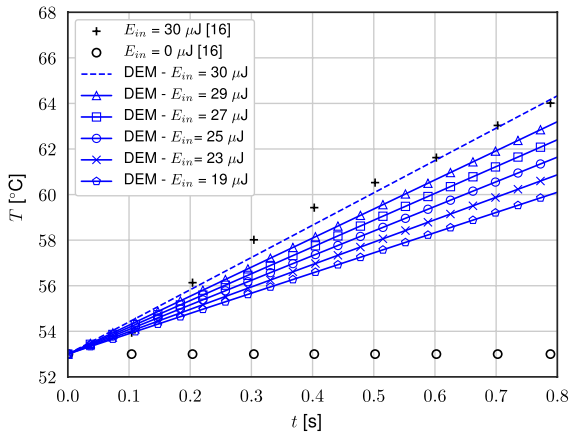


**Fig. 14** Temperature evolution while sintering PS particle pairs. Initial temperature is set to $T_0 = 53$ °C. Cross markers correspond to the data extracted from [21], while the dashed and marked lines are the DEM simulation results

of $\mu = 270$ Pa s. Our proposed model evidences a better approximation during the whole process.

Similarly to PA12 particles, the simulations of PS pairs using the calibrated parameters reported in Table 5 are visualized in Figs. 13 and 15.

As visualized in Fig. 13, faster sintering and higher interpenetration are achieved when higher laser intensities are

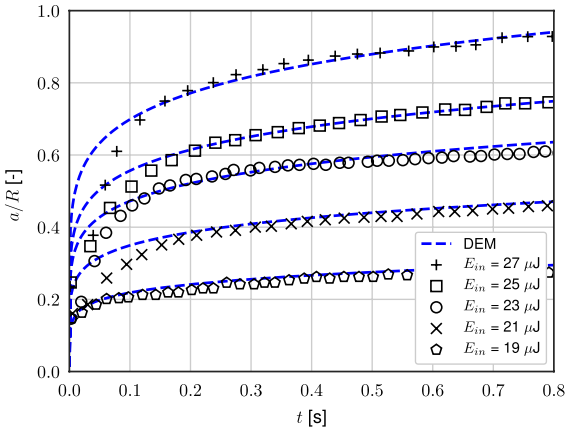


**Fig. 15** Neck growth of PS particle pairs as a function of time, for different applied laser energies. The dashed lines correspond to calibrated DEM simulations, symbols are the experimental data from [21]

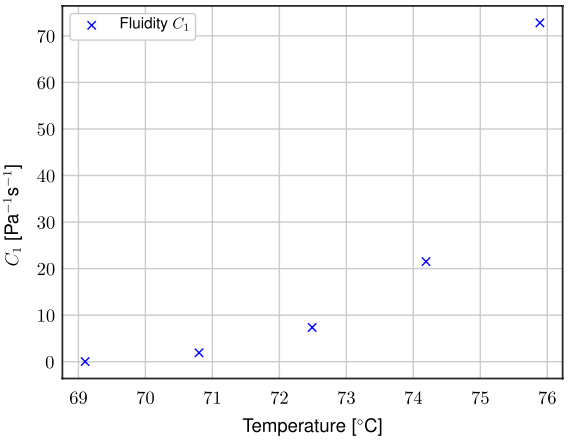


**Fig. 16** Temperature-dependent fluidity values, $C_1$, of PS

applied. The laser hits the interface of the particles at $t = 0$ s, and the neck is formed which tends to grow up to the pulse duration of the laser beam at 0.8 s. Following the absorption analysis and experimental information, irradiating 27 $\mu$J on PS particle surface leads to the absorption of 93.7% of the incident energy. The energy absorbed under the different laser setups is summarized in Table 6.

The absorption analysis suggests that PS reflects around 6% of the incoming energy, which is 1% more than predicted by Hejmady et al. [21]; the authors measured absorption on a flat polymeric surface.

The simulation result of the temperature evolution on PS particle pairs is presented in Fig. 14.

According to the experimental set-up, the sintering of PS particle pairs occurs slow and principally during the heating stage ($t < 0.8$ s). The DEM simulation and the absorption analysis predict the window in which the temperature evolves as a function of the irradiated laser energy, as reported by Hejmady et al. [21].

Subsequently, the evolution of the neck radius as a function of time is determined through particle-particle overlap. The result is presented in Fig. 15.

Figure 15 shows the effect of laser energy on the sintering of particle pairs, which is maximum for the case of $E_{in} = 27$ $\mu$J that leads to overlap of the particles of 90%; it reduces to around 25% when decreasing the irradiated energy to $E_{in} = 19$ $\mu$J. The stress relaxation for flowability is achieved almost instantaneously after the consolidation starts, letting surface tension dominate the process. This behaviour is expected since PS powders sinter faster compared to other polymers [25]. These simulations of particle pairs reveal the influence of the laser energy on the achieved neck radius. For the design of sintering procedures, a lower limit for solid-state sintering would be desirable ($a/R > 0.7$) to avoid breakage. A deviation in the simulations and experimental data is evidenced in the early stage $t < 0.1$ s. One possible reason could be the recording process that limits measurements in short time frames.

Crystallization can occur during cooling if the rate of temperature decrease is too high, especially for semi-crystalline materials such as PS. Whereas the material contact rheology determines the kinetics of the sintering of the neck region, the crystallization kinetics will affect the solidification. We have neglected in our model any crystallization effect for brevity, and future studies can discuss crystallization models to describe the aforementioned phase, such as the proposed by Shen et al. [37].

Raising the laser power also enhances the flowability of the particles, a trend supported by the model parameter fluidity denoted as $C_1$, which exhibits a notable increase with the rise in irradiated energy. This relationship between fluidity $C_1$ and Temperature is depicted in Fig. 16.

As the temperature within a polymer increases, the thermal energy of the polymer chains also increases, leading to an increase in the kinetic energy of the molecules. This causes the polymer chains to vibrate more vigorously and move more freely, which in turn reduces the entanglement and cross-linking of the chains. This decrease in intermolecular forces reduces the viscosity of the polymer and increases its fluidity as illustrated in Fig. 16. The relationship between temperature and fluidity of polymers near their melting point can depend on several factors, including the specific polymer and its properties, such as molecular weight, degree of branching, and presence of cross-linking. Additionally, the conditions under which the polymer is being heated or cooled can affect its behaviour, including the heating rate and duration, as well as the cooling rate. However, these details are beyond the scope of this study.

## 5 Conclusions and outlook

In this study, we developed a numerical approach utilising the discrete element method (DEM) to analyse the laser sintering process with a specific emphasis on neck growth contact rheology. This approach was integrated into the MercuryDPM software package.

First, we collected reported experimental data related to laser sintering. The experiments recorded the neck growth and temperature evolution of PA12 and PS particle pairs undergoing sintering via laser beam; for PA12, this occurred above the melting point, whereas for PS, it took place above the glass transition temperature.

Second, we developed a multi-physics DEM model. This model accounted for the intricate thermal energy balance resulting from particle contact with thermal disruption, including mechanisms such as conduction, convection, and radiation. Additionally, we incorporated the external influence of a laser beam through a ray tracing approach. To enhance the capability of our model, we introduced a novel sintering description that encompasses three distinct mechanisms to simulate the contact rheology of visco-elastic particles.

Finally, guided by the experimental data, we conducted simulations using the GrainLearning package. These simulations required the calibration of model parameters, including surface tension, stiffness, thermal convection, emissivity, and fluidity. The outcomes of these simulations presented good agreement with the temperature evolution recorded experimentally, as well as the dependence of energy absorption on facilitating neck growth on the particle pairs. Notably, our investigation revealed that fluidity, a key parameter controlling sintering rates, exhibited an increasing behaviour concerning high temperatures. This suggests that the dominance of the flow phase, driven by surface tension, mitigates geometric variations, such as thermal expansion. It is important to note that the performance of our DEM model may vary for different materials, such as metals or ceramics, and further evaluation can be conducted to assess its predictive capabilities across diverse materials.

The experimental results indicated that low contact pressure did not diminish heat conductance; instead, it showcased the efficiency of the materials to conduct heat. Several contributing factors were identified, including localised heating that precisely defined the sintering zone, concentrating heat in specific regions, and optimising the overall efficiency of the sintering process. The laser beam's high energy density facilitated in accelerating the heating process, promoting rapid absorption, and enhancing heat conductance. Additionally, the reduced thermal inertia associated with small particle size enhanced faster temperature changes, contributing to efficient heat transfer during sintering.

Furthermore, the experiments revealed that radiation played a negligible role due to the limited temperature difference between particles and the heating chamber. Controlled atmospheric conditions mitigated the relevance of fluid flow, while the rearrangement of particles either by thermal expansion or contraction did not adversely affect the results, given the configuration setup and particle characteristics.

Further work can focus on exploring the influence of different mechanical properties like crystallinity, and particle properties such as particle size, poly-disperse size distributions, and the bulk volume fraction on sintering. Additionally, exploring changes in material properties, for example friction as a function of temperature, could enhance the model's accuracy, particularly near phase transitions, where such variations may significantly influence particle interactions and sintering behaviour.

**Acknowledgements** This work was financially supported by NWO-TTW project No.16604 Virtual Prototyping of Particulate Processes (ViPr) Design and Optimisation via Multi-scale Modelling and Rapid Prototyping.

## Declarations

**Conflict of interest** The authors have no competing interests to declare that are relevant to the content of this article.



## References

1. Ligon, S.C., Liska, R., Stampfl, J., Gurr, M., Mülhaupt, R.: Polymers for 3D printing and customized additive manufacturing. Chem. Rev. **117**(15), 10212–10290 (2017). https://doi.org/10.1021/acs.chemrev.7b00074
2. Rando, P., Ramaioli, M.: Numerical simulations of sintering coupled with heat transfer and application to 3D printing. Addit. Manuf. **50**, 102567 (2022). https://doi.org/10.1016/j.addma.2021.102567
3. Meng, Q., Song, X., Han, S., Abbassi, F., Zhou, Z., Wu, B., Wang, X., Araby, S.: Mechanical and functional properties of polyamide/graphene nanocomposite prepared by chemicals free-approach and selective laser sintering. Compos. Commun. **36**, 101396 (2022). https://doi.org/10.1016/j.coco.2022.101396
4. Sassaman, D.M., Ide, M.S., Beaman, J.J., Kovar, D.: A model for bonding mechanisms in indirect laser powder bed fusion of nylon/alumina blends. Addit. Manuf. **59**, 103163 (2022). https://doi.org/10.1016/j.addma.2022.103163

5. Bierwisch, C., Mohseni-Mofidi, S., Dietemann, B., Gruenewald, M., Rudloff, J., Lang, M.: Universal process diagrams for laser sintering of polymers. Mater. Design **199**, 109432 (2021). https://doi.org/10.1016/j.matdes.2020.109432
6. Dorussen, B.J., Geers, M.G., Remmers, J.J.: A discrete element framework for the numerical analysis of particle bed-based additive manufacturing processes. Engi. Comput. **38**, 1–16 (2022). https://doi.org/10.1007/s00366-022-01631-8
7. Ganeriwala, R., Zohdi, T.I.: A coupled discrete element-finite difference model of selective laser sintering. Granul. Matter **18**(2), 21 (2016). https://doi.org/10.1007/s10035-016-0626-0
8. Shinagawa, K.: Simulation of grain growth and sintering process by combined phase-field/discrete-element method. Acta Mater. **66**, 360–369 (2014). https://doi.org/10.1016/j.actamat.2013.11.023
9. Nosewicz, S., Rojek, J., Chmielewski, M., Pietrzak, K., Lumelskyj, D.: Application of the Hertz formulation in the discrete element model of pressure-assisted sintering. Granul. Matter **19**, 1–8 (2017). https://doi.org/10.1007/s10035-016-0699-9
10. Mukherjee, T., Zhang, W., DebRoy, T.: An improved prediction of residual stresses and distortion in additive manufacturing. Comput. Mater. Sci. **126**, 360–372 (2017). https://doi.org/10.1016/j.commatsci.2016.10.003
11. Balemans, C., Hulsen, M.A., Anderson, P.D.: On the validity of 2D analysis of non-isothermal sintering in SLS. Chem. Eng. Sci. **213**, 115365 (2020). https://doi.org/10.1016/j.ces.2019.115365
12. Körner, C., Osmanlic, F., Drummer, D., Wudy, K., Laumer, T., Schmidt, M.: Modeling of laser beam absorption in a polymer powder bed. Polymers **10**(7), 784 (2018). https://doi.org/10.3390/polym10070784
13. Dong, L., Makradi, A., Ahzi, S., Remond, Y., Sun, X.: Simulation of the densification of semicrystalline polymer powders during the selective laser sintering process: Application to nylon 12. Polym. Sci., Ser. A **50**(6), 704–709 (2008). https://doi.org/10.1134/S0965545X0806014X
14. Hejmady, P., Breemen, L.C., Hermida-Merino, D., Anderson, P.D., Cardinaels, R.: Laser sintering of PA12 particles studied by in-situ optical, thermal and X-ray characterization. Addit. Manuf. **52**, 102624 (2022). https://doi.org/10.1016/j.addma.2022.102624
15. Polychronopoulos, N.D., Sarris, I.E., Vlachopoulos, J.: A viscous sintering model for pore shrinkage in packings of cylinders. Rheol. Acta **60**(8), 397–408 (2021). https://doi.org/10.1007/s00397-021-01279-z
16. Luding, S., Manetsberger, K., Müllers, J.: A discrete model for long time sintering. J. Mech. Phys. Solids **53**(2), 455–491 (2005). https://doi.org/10.1016/j.jmps.2004.07.001
17. Luding, S.: Cohesive, frictional powders: contact models for tension. Granul. Matter **10**(4), 235–246 (2008). https://doi.org/10.1007/s10035-008-0099-x
18. Peng, Z., Doroodchi, E., Moghtaderi, B.: Heat transfer modelling in discrete element method (DEM)-based simulations of thermal processes: theory and model development. Prog. Energy Combust. Sci. **79**, 100847 (2020). https://doi.org/10.1016/j.pecs.2020.100847
19. Li, S., Marshall, J.S., Liu, G., Yao, Q.: Adhesive particulate flow: the discrete-element method and its application in energy and environmental engineering. Prog. Energy Combust. Sci. (2011). https://doi.org/10.1016/j.pecs.2011.02.001
20. Pokluda, O., Bellehumeur, C.T., Vlachopoulos, J.: Modification of Frenkel's model for sintering. AIChE J. **43**(12), 3253–3256 (1997). https://doi.org/10.1002/aic.690431213
21. Hejmady, P., Van Breemen, L.C.A., Anderson, P.D., Cardinaels, R.: Laser sintering of polymer particle pairs studied by in situ visualization. Soft Matter **15**(6), 1373–1387 (2019). https://doi.org/10.1039/C8SM02081G
22. Cheng, H., Shuku, T., Thoeni, K., Tempone, P., Luding, S., Magnanimo, V.: An iterative Bayesian filtering framework for fast and automated calibration of DEM models. Comput. Methods Appl. Mech. Eng. **350**, 268–294 (2019). https://doi.org/10.1016/j.cma.2019.01.027
23. Hartmann, P., Cheng, H., Thoeni, K.: Performance study of iterative Bayesian filtering to develop an efficient calibration framework for DEM. Comput. Geotech. **141**, 104491 (2022). https://doi.org/10.1016/j.compgeo.2021.104491
24. Weinhart, T., Orefice, L., Post, M., van Schrojenstein Lantman, M.P., Denissen, I.F.C., Tunuguntla, D.R., Tsang, J.M.F., Cheng, H., Shaheen, M.Y., Shi, H., Rapino, P., Grannonio, E., Losacco, N., Barbosa, J., Jing, L., Alvarez Naranjo, J.E., Roy, S., Otter, W.K., Thornton, A.R.: Fast, flexible particle simulations: an introduction to MercuryDPM. Comput. Phys. Commun. **249**, 107129 (2020). https://doi.org/10.1016/j.cpc.2019.107129
25. Alvarez, J., Snijder, H., Vaneker, T., Cheng, H., Thornton, A., Luding, S., Weinhart, T.: Visco-elastic sintering kinetics in virgin and aged polymer powders. Powder Technol. **397**, 117000 (2022). https://doi.org/10.1016/j.powtec.2021.11.044
26. Kang, S.J.L.: Sintering: Densification. Grain Growth and Microstructure. Elsevier Science, Korea (2004). https://doi.org/10.1016/B978-0-7506-6385-4.X5000-6
27. Johnson, K., Kendall, K., Roberts, A.: Surface energy and the contact of elastic solids. Proc. R. Soc. Lond. A. Math. Phys. Sci. **324**(1558), 301–313 (1971). https://doi.org/10.1098/rspa.1971.0141
28. Frenkel, J.: Viscous flow of crystalline bodies under the action of surface tension. J. Phyis. **9**, 385 (1945)
29. Yaagoubi, H., Abouchadi, H., Taha Janan, M.: Simulation of the heat laser of the selective laser sintering process of the polyamide 12. E3S Web Conf. **297**, 01050 (2021). https://doi.org/10.1051/e3sconf/202129701050
30. Sultanova, N., Kasarova, S., Nikolov, I.: Dispersion proper ties of optical polymers. Acta Physica Polonica-Ser. A Gen. Phys. **116**(4), 585 (2009). https://doi.org/10.12693/APhysPolA.116.585
31. Berretta, S., Wang, Y., Davies, R., Ghita, O.R.: Polymer viscosity, particle coalescence and mechanical performance in high-temperature laser sintering. J. Mater. Sci. **51**(10), 4778–4794 (2016). https://doi.org/10.1007/s10853-016-9761-6
32. Rohsenow, W.M., Hartnett, J.P., Cho, Y.I.: Handbook of Heat Transfer. McGraw-Hill New York, US (1998). https://www.accessengineeringlibrary.com/content/book/9780070535558
33. Ganeriwala, R., Zohdi, T.I.: Multiphysics modeling and simulation of selective laser sintering manufacturing processes. Procedia Cirp **14**, 299–304 (2014). https://doi.org/10.1016/j.procir.2014.03.015
34. Lin, Y.Y., Hui, C.Y., Jagota, A.: The role of viscoelastic adhesive contact in the sintering of polymeric particles. J. Colloid Interface Sci. **237**(2), 267–282 (2001). https://doi.org/10.1006/jcis.2001.7470
35. Bellehumeur, C.T., Kontopoulou, M., Vlachopoulos, J.: The role of viscoelasticity in polymer sintering. Rheol. Acta **37**(3), 270–278 (1998). https://doi.org/10.1007/s003970050114
36. Zhao, M., Drummer, D., Wudy, K., Drexler, M.: Sintering study of polyamide 12 particles for selective laser melting. Int. J. Recent Contrib. Eng. Sci. IT (iJES) **3**(1), 28 (2015). https://doi.org/10.3991/ijes.v3i1.4290
37. Shen, F., Zhu, W., Zhou, K., Ke, L.-L.: Modeling the temperature, crystallization, and residual stress for selective laser sintering of polymeric powder. Acta Mech. **232**(9), 3635–3653 (2021). https://doi.org/10.1007/s00707-021-03020-6